

# Spatiotemporal tomography based on scattered multiangular signals and its application for resolving evolving clouds using moving platforms

Roi Ronen, Yoav Y. Schechner  
Viterbi Faculty of Electrical Engineering  
Technion - Israel Institute of Technology  
Haifa, Israel

roironen@campus.technion.ac.il  
yoav@ee.technion.ac.il

Eshkol Eytan  
Department of Earth and Planetary Sciences  
The Weizmann Institute of Science  
Rehovot, Israel

eshkol.eytan@weizmann.ac.il

## Abstract

We derive computed tomography (CT) of a time-varying volumetric translucent object, using a small number of moving cameras. We particularly focus on passive scattering tomography, which is a non-linear problem. We demonstrate the approach on dynamic clouds, as clouds have a major effect on Earth's climate. State of the art scattering CT assumes a static object. Existing 4D CT methods rely on a linear image formation model and often on significant priors. In this paper, the angular and temporal sampling rates needed for a proper recovery are discussed. If these rates are used, the paper leads to a representation of the time-varying object, which simplifies 4D CT tomography. The task is achieved using gradient-based optimization. We demonstrate this in physics-based simulations and in an experiment that had yielded real-world data.

## 1. Introduction

Computed tomography (CT) is a powerful way to recover the inner structure of three dimensional (3D) volumetric heterogeneous objects [16]. Being possibly one of the earliest types of computational photography methods, CT has extensive use in many research and operational domains. These include medicine [41], sensing of atmospheric pollution [4], geophysics [49] and fluid dynamics [51,52]. As a result, CT technologies and novel modalities are increasingly being advanced by the computer vision and graphics communities [18,38].

CT requires imaging from multiples directions [5,24]. In nearly all CT approaches, the object is considered static during image acquisition. However, in many cases of interest, the object changes while multi-view images are acquired sequentially [11,53]. Thus, effort has been invested

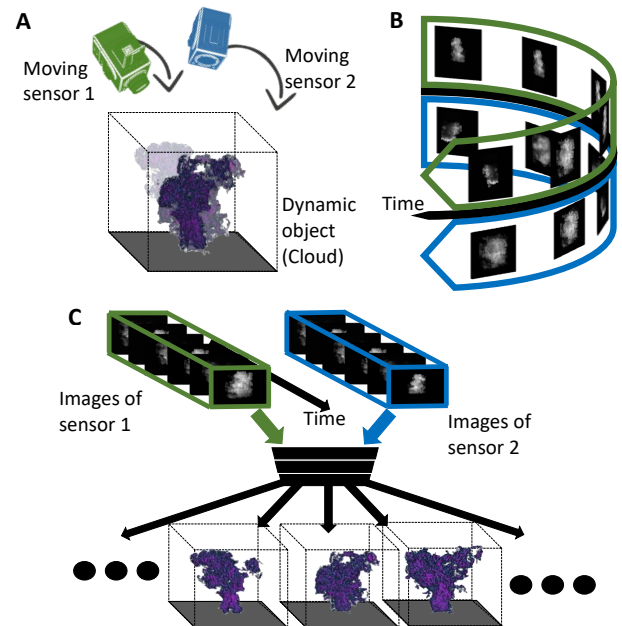


Figure 1: [A] Multiple moving sensors scan a time-varying object (cloud) from multiple-views. [B] The measurements, acquired at a different times, are the input to our method, which aims to recover the 3D volume density of the object at the different times [C].

to generalize 3D CT to four-dimensional (4D) spatiotemporal CT, particularly in the computer vision and graphics communities [42,52,53]. This effort has been directed at linear-CT modalities. Linear CT is computationally easier to handle, thus common for decades, mainly in medical imaging [22]. Medical CT often exploited the periodic temporal nature of organ dynamics, to synchronize sequen-

tial acquisitions [41]. The generalization in linear CT is mirrored in a generalization of object surface recovery by spatio-temporal computer vision [28, 37, 42].

This paper focuses on a more complicated model: scattering CT. It is important to treat this case for scientific, societal and practical reasons. The climate is strongly affected by interaction with clouds [15] (Fig. 1).

To reduce major errors in climate predictions, this interaction requires a much finer understanding of cloud physics than current knowledge. Current knowledge is based on empirical remote sensing data that is analyzed under the assumption that the atmosphere and clouds are made of very broad and uniform layers. This leads to errors in climate understanding. To overcome this problem, 3D scattering CT has been suggested as a way to study clouds [30, 31].

Scattering CT of clouds requires high resolution multi-view images from space. There are spaceborne and high-altitude systems may provide such data, such as AirM-SPI [10], MAIA [7], HARP [40], AirHARP [36] and the planned CloudCT formation [43]. However, there is a practical problem: these systems are very expensive, so it is not realistic to deploy them in large numbers to simultaneously acquire images of the same clouds from many angles. Therefore, in practice, the platforms are planned to move above the clouds: a sequence of images is taken, in order to span and sample a wide angular breadth, but the cloud evolves meanwhile. Hence there are important reasons to derive 4D scattering CT, particularly of clouds.

We pose conditions under which this task can be performed. These relate to temporal sampling and angular breadth, in relation to the correlation time of the evolving object. Then, we generalize prior 3D CT, specifically scattering CT, to spatiotemporal recovery using data taken by moving cameras. We present an optimization-based method to reach this, and then demonstrate this method both in rigorous simulations and on real data.

## 2. Theoretical Background

Computed Tomography (CT) seeks estimation of the 3D volumetric density of  $\beta$  an object. Usually, CT measures the object from multiple directions. Denote those measurements by  $\mathbf{y}$ . A forward model  $\mathcal{F}(\beta)$  expresses the image formation model. Estimation of  $\beta$  is done by minimization of a cost  $\mathcal{E}$ , which penalizes the discrepancy between  $\mathbf{y}$  and the forward model,

$$\hat{\beta} = \underset{\beta}{\operatorname{argmin}} \mathcal{E}[\mathbf{y}, \mathcal{F}(\beta)] . \quad (1)$$

Often, acquiring data from multiple angles simultaneously is very difficult. Sensors are expensive and/or power-consuming. Thus, their duplication in large numbers to sample many directions is often prohibitive. Sometimes the sensors are bulky and need cooling, posing difficulty

to pack them densely. Therefore, CT measurements are often acquired *sequentially*. In contrast, the inverse tomographic problem (Eq. 1) expresses the object as time-invariant. However, in many situations it is not the case; the object changes in time. Thus, modeling the inverse problem as Eq. (1) is inconsistent both with the dynamic nature of the object and the sequential nature of the sensing process.

This paper focuses on scattering-based CT. Thus, we describe here the relevant forward model. We follow notations and definitions of [4, 30]. Material density at a voxel is denoted by  $\beta$ . In case the main interaction effect is scattering (rather than absorption or emission), as is the case of visible light in clouds,  $\beta$  is the extinction or scattering coefficient of the medium, in units of  $\text{km}^{-1}$ . Concatenating this coefficient in all voxels creates a vector  $\beta_t$ , per time  $t$ . The interaction of radiation with a scattering volumetric object is modeled by 3D *radiative transfer*, which includes multiple scattering. Define radiative transfer by an operator  $\text{RT}(\beta_t)$ . There are various algorithms to implement  $\text{RT}(\beta_t)$ , including Monte-Carlo [33, 35] and the spherical harmonic discrete ordinate method (SHDOM). We use the latter, as it is considered trustworthy by the scientific community [12] and has open-source online codes [29].

Radiative transfer yields the radiance  $i(\mathbf{x}, \omega)$  at each location  $\mathbf{x}$  in space and each light propagation direction  $\omega$ . A camera observes the scene from a specific location, while each of the camera pixels samples a direction  $\omega$ . Hence, imaging (forward model) amounts to sampling the output of radiative transfer at the camera locations and pixels' lines of sight, while integrating over the camera exposure time and spectral bands. Camera sampling is denoted by a projection operator  $P_{\mathbf{x}, \omega}$ . To conclude, the forward model for the expected value of a pixel gray level at time  $t$  is

$$g_{\mathbf{x}, \omega, t} = \mathcal{F}(\beta_t) \approx \gamma^{\text{cam}} P_{\mathbf{x}, \omega} \{ \text{RT}(\beta_t) \} . \quad (2)$$

Here  $\gamma^{\text{cam}}$  expresses camera properties, including the lens aperture area, exposure time, spectral band, quantum efficiency and lens transmissivity. Eq. (2) assumes that the exposure time is sufficiently small, such that within this time, the scene and the camera pose vary insignificantly.

Empirical measurements include random noise. The noise mainly originates from the discrete nature of photons and electric charges, which yields a Poisson process. There are additional noise sources, and their parameters can be extracted from the sensor specifications. Denote incorporation of noise into the expected signal by the operator  $\mathcal{N}$ . Then, a raw measurement is

$$y_{\mathbf{x}, \omega, t} = \mathcal{N} \{ g_{\mathbf{x}, \omega, t} \} . \quad (3)$$

## 3. Representing Dynamic Volumetric Objects

In this section, we present an approximate representation of volumetric 3D objects, which evolve gradually in

time. There is a need and justification for the approximation. The need is because in our work, there is often insufficient simultaneous data for high quality 3D tomography at all times. Data is captured sequentially, while the object evolves. Hence, at best, we would recover a good approximation of the evolving object. The approximation can be satisfactory, however, if temporal samples are sufficiently dense, as elaborated in Sec. 4.

The object has an evolving state, which is sampled at the time set  $\mathcal{T} = \{t_1, t_2, \dots, t_{N^{\text{state}}}\}$ . At time  $t \in \mathcal{T}$ , the true object is represented by the instantaneous 3D extinction field  $\beta_t$ . Define a corresponding hidden field  $\beta_t^{\text{hidden}}$ . The instantaneous field is represented as a convex linear combination of the hidden fields:

$$\beta_t = \sum_{t' \in \mathcal{T}} w_t(t') \beta_{t'}^{\text{hidden}}. \quad (4)$$

All weights  $\{w_t(t')\}$  satisfy  $0 \leq w_t(t') \leq 1$  and

$$\sum_{t' \in \mathcal{T}} w_t(t') = 1. \quad (5)$$

Equation (4) implies a non-negative correlation of the 3D field at  $t$  to the 3D field at any time  $t'$ . Correlation should decay with the time lag  $|t - t'|$ . We set the weights by a normal function

$$w_t(t') = s \exp\left(-\frac{|t - t'|^2}{2\sigma^2}\right). \quad (6)$$

Here  $s$  is a normalization factor, set to satisfy Eq. (5).

The parameter  $\sigma$  expresses the *effective correlation time* of the volumetric object. We elaborate on the value of  $\sigma$  in Sec. 4. Two limiting cases are illustrative, however. For  $\sigma \rightarrow \infty$ , we have  $w_t(t') \rightarrow 1/N^{\text{state}}$ . This means that the object  $\beta$  is effectively static. On the other hand, for  $\sigma \rightarrow 0$ , we have  $w_t(t') \rightarrow \delta(t - t')$ , i.e. a Dirac delta function. This means that the object  $\beta$  varies so fast, that at any time  $t$  its state is uncorrelated to the state at other times.

## 4. Bandwidth and Object Sampling

In Sec. 3, a 3D volumetric object which gradually evolves is represented using a linear superposition of sampled states. The linear superposition is controlled by a kernel, whose width is  $\sigma$ . Here we elaborate both on the sampling process and how  $\sigma$  emerges from the temporal nature of the object. The relation between a continuously varying object and its discrete temporal samples is governed by the Nyquist sampling theorem. This theorem states, that for an infinite time domain:

- Sampling loses no information if for any time sample index  $k$ ,  $|t_{k+1} - t_k| \leq (2B)^{-1}$ , where  $B$  is the half-bandwidth of the object's temporal variations.

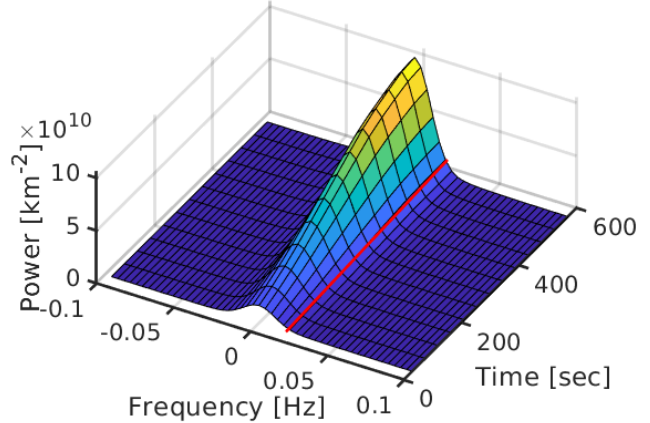


Figure 2: A cutoff frequency  $\approx 1/50[\text{Hz}]$ , within which 95% of the signal power is contained, is marked in red.

- Based on these lossless temporal samples, lossless reconstruction of the object is achieved by a linear superposition of the samples. The linear superposition is achieved by temporal convolution of the samples with a sinc kernel. This kernel has infinite temporal length. The kernel's effective half-width, defined by its first zero-crossing, is  $(2B)^{-1}$ .

In practice, the temporal domain, number of samples and reconstruction kernels are finite. Moreover, the object's temporal spectrum is often not completely band-limited by  $B$ , because some low energy content has far higher frequencies. Consequently, sampling and reconstruction are lossy, yielding an approximate result. The reconstruction is not performed by a sinc kernel, but using a finite-length kernel, such as the cropped Gaussian  $w_t(t')$  of Eq. (6). Correspondingly, in our approximation,  $\sigma \sim (2B)^{-1}$ .

As an example, consider warm convective clouds. They are governed by air turbulence of decameter scale. In these scales [15], the *correlation time* of content in a voxel is about  $\approx 20$  to 50 seconds. This indicates that *4D spatiotemporal clouds can be recovered well using 4D spatiotemporal samples*, if the temporal samples are about 30 seconds apart. Furthermore, this indicates the range of values of  $\sigma$ . Moreover, the entire lifetime of a warm convective cloud is typically measured in minutes.

An additional illustration is given by a cloud simulation, which is described in detail in Sec. 7.1. The cloud evolves for about 10 minutes. For each cloud voxel, we calculated the power spectrum using the short-time Fourier transform. This power was then aggregated over all voxels. The total temporal spectrum is plotted in Fig 2. The spectrum is effectively limited. The cutoff is not sensitive to evolving stages of the clouds. From this cutoff, a temporal sampling period which is 25[sec] or shorter encapsulates most of the energy of the temporal variations. Hence, we set  $\sigma \approx 25[\text{sec}]$  for clouds.

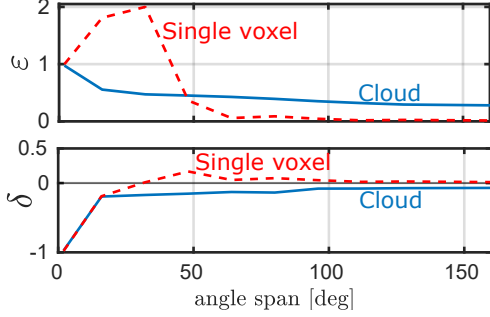


Figure 3: A static heterogeneous cloud and a single-voxel cloud (having size  $20\text{m} \times 20\text{m} \times 20\text{m}$ ) are recovered from nine viewpoints. The plots are of errors defined in Eq. (8).

## 5. Tomographic Angular Extent

Section 4 dealt with sampling of an object, as if 4D measurements are done in-situ. However, in CT, we have no direct access to  $\beta_t$ : we only measure projections  $\mathbf{y}_t$ . As we discuss now, projections must have a *wide angular breadth*, while object evolution is small.

Consider an extreme case. Let a cloud be temporally constant and reside only in a single voxel, over the ocean. Viewed from space by two cameras simultaneously, cloud recovery here amounts to triangulation. In triangulation, the best cloud-localization resolution is obtained if the angular range between the two cameras is  $90^\circ$ . At small baselines, localization decreases linearly with the decreasing angular extent. When more than two cameras operate, localization behaves more moderately, but with a similar trend. Consider two criteria that had been used in 3D CT [23, 30, 33]. Per time sample  $t$ ,

$$\delta_t = \frac{\|\beta_t^{\text{true}}\|_1 - \|\hat{\beta}_t\|_1}{\|\beta_t^{\text{true}}\|_1}, \quad \varepsilon_t = \frac{\|\beta_t^{\text{true}} - \hat{\beta}_t\|_1}{\|\beta_t^{\text{true}}\|_1} \quad (7)$$

relate, respectively, to the relative bias of the object mass and the relative recovery error. We generalize them to the whole sample set  $t \in \mathcal{T}$ , by averaging:

$$\delta = \frac{1}{N_{\text{state}}} \sum_{t \in \mathcal{T}} \delta_t, \quad \varepsilon = \frac{1}{N_{\text{state}}} \sum_{t \in \mathcal{T}} \varepsilon_t. \quad (8)$$

Fig. 3 plots the measures when CT attempts to recover a single-voxel cloud (extending 20 meters), when 9 cameras surround it from 500km away. Above  $\approx 60^\circ$  total angular extent, recovery reaches a limiting excellent quality, but quality is very poor at narrow angle spans.

What happens in extended objects? In linear-CT (as in medical X-ray CT), information loss due to limited-angle imaging is known as the *missing cone of frequencies* [2, 34]. In scattering CT, with the exception of very sparse objects, the missing cone linear theory does not apply. However (See Fig. 3), there is a marked degradation of quality if

the angular extent is narrow. Here, scattering CT is performed on a single-state (fixed time) of a cloud simulated as in Sec. 7.1.

So far, this section dealt with static clouds. Clouds are considered nearly static between times  $t, t'$  if  $|t - t'| < \sigma$ . The viewing angular extent covered in those times (and in intermediate times) is denoted  $\Theta(t, t')$ , in radians. So, within time span  $\approx \sigma$  good recovery can be achieved only if  $2\Theta(t, t')/\pi$  is large. If it is low, then spatial (altitude) resolution in CT recovery is lost. Most CT systems cover wide angular extent, eventually. So, guarantee for quality is the angular rate. Define a dimensionless figure

$$\rho = \frac{2\Theta(t, t')}{\pi} \frac{\sigma}{|t - t'|}. \quad (9)$$

Good 4D recovery requires  $\rho \gtrsim 1$ , while temporal sampling satisfies the condition of Sec. 5. The more these conditions are violated, the worse 4D CT is expected to perform.

## 6. 4D Scattering Tomography

We now generalize Eq. (1) to 4D CT. At any time  $t \in \mathcal{T}$ , the object is viewed simultaneously from a set of viewpoints  $\mathcal{C}_t$ . The image data captured in viewpoint  $c \in \mathcal{C}_t$  is denoted by the vector  $\mathbf{y}_c$ . The image data captured simultaneously by all cameras  $c \in \mathcal{C}_t$  is concatenated to a vector  $\mathbf{y}_t$ . At that time, the modeled medium variables are represented by a vector  $\beta_t$ . At the corresponding time, as described in Sec. 3, there is a hidden representation of the medium,  $\beta_t^{\text{hidden}}$ .

The inverse problem is now formulated by

$$\{\hat{\beta}_t\}_{t \in \mathcal{T}} = \arg \min_{\{\beta_t\}_{t \in \mathcal{T}}} \sum_{t \in \mathcal{T}} \mathcal{E}[\mathbf{y}_t, \mathcal{F}(\beta_t)]. \quad (10)$$

We use

$$\mathcal{E}[\mathbf{y}_t, \mathcal{F}(\beta_t)] = \frac{1}{2} \|\mathbf{y}_t - \mathcal{F}(\beta_t)\|_2^2. \quad (11)$$

Eq. (10) can be solved efficiently by gradient-based methods. Towards this, let us approximate the gradient of the cost being minimized in Eq. (10) by

$$\frac{\partial}{\partial \beta_t} \sum_{t' \in \mathcal{T}} \mathcal{E}[\mathbf{y}_{t'}, \mathcal{F}(\beta_{t'})] \approx \frac{\partial}{\partial \beta_t^{\text{hidden}}} \sum_{t' \in \mathcal{T}} \mathcal{E}[\mathbf{y}_{t'}, \mathcal{F}(\beta_{t'})]. \quad (12)$$

Note that

$$\begin{aligned} \frac{\partial}{\partial \beta_t^{\text{hidden}}} \sum_{t' \in \mathcal{T}} \mathcal{E}[\mathbf{y}_{t'}, \mathcal{F}(\beta_{t'})] &= \\ \sum_{t' \in \mathcal{T}} \frac{\partial \mathcal{E}[\mathbf{y}_{t'}, \mathcal{F}(\beta_{t'})]}{\partial \beta_{t'}} \frac{\partial \beta_{t'}}{\partial \beta_t^{\text{hidden}}}. \end{aligned} \quad (13)$$

From Eq. (11),

$$\frac{\partial \mathcal{E}[\mathbf{y}_{t'}, \mathcal{F}(\beta_{t'})]}{\partial \beta_{t'}} = [\mathcal{F}(\beta_{t'}) - \mathbf{y}_{t'}] \frac{\partial \mathcal{F}(\beta_{t'})}{\partial \beta_{t'}}, \quad (14)$$

while from Eq. (4),

$$\frac{\partial \beta_{t'}}{\partial \beta_t^{\text{hidden}}} = w_{t'}(t). \quad (15)$$

Define the set of medium density fields at all sampled times  $\mathcal{B} = \{\beta_{t'}\}_{t' \in \mathcal{T}}$ . From Eqs. (12,13,14,15), for optimizing the field at time  $t$ , the approximate gradient is

$$\mathbf{g}_t(\mathcal{B}) = \sum_{t' \in \mathcal{T}} w_{t'}(t) [\mathcal{F}(\beta_{t'}) - \mathbf{y}_{t'}] \frac{\partial \mathcal{F}(\beta_{t'})}{\partial \beta_{t'}}. \quad (16)$$

A gradient-based approach then performs per iteration  $k$ :

$$\beta_t(k+1) = \beta_t(k) - \alpha \mathbf{g}_t(\mathcal{B}_k) \quad (17)$$

where  $\alpha$  is a step size and  $\mathcal{B}_k = \{\beta_{t'}(k)\}_{t' \in \mathcal{T}}$ .

The approach in Eqs. (10-17) is not specific to scattering CT. The formulation *can apply generically to other inverse problems* where data is acquired sequentially while the object evolves, and the forward model  $\mathcal{F}$  is known and differentiable. In case of scattering CT,  $\mathcal{F}$  is discussed in Sec. 2. Computing the Jacobian  $\partial \mathcal{F}(\beta_{t'}) / \partial \beta_{t'}$  is complex then. However, there are approximations to the Jacobian of 3D RT, which can be computed efficiently [30, 33], making the recovery tractable. The complexity of solving Eq. (10) is similar to 3D static CT by (1). We performed optimization using a L-BFGS-B solver [54].

Following [31], prior to the optimization process, the set of voxels to estimate is bounded using space-carving [27]. Space-carving bounds a 3D shape by back-projecting multi-view images. A voxel is labeled as belonging to the object, if the number of back-projected rays that intersect this voxel is greater than a threshold. To adapt this approach to our dynamic framework, the shape was estimated in a coarse spatial grid and using a low threshold for labeling voxels as potentially part of the cloud.

## 7. Simulations

We test the proposed method on clouds. The atmosphere is a scattering medium which changes continuously. It includes several types of scattering particles, including water droplets, aerosols and molecules. Scattering by water droplets is usually much more dominant and spatiotemporally variable than aerosols, hence we focus on the former. Scattering by air molecules does not require imaging: it follows Rayleigh theory. Molecular density changes mainly in height and is usually known globally using non-imaging sensors. Thus, the evolving concentration of cloud water droplets is the main unknown we sense and seek.

### 7.1. Cloud Simulation

For realistic complexity, we use a rigorous simulation based on cloud physics, including evolution of the cloud

microphysics. Clouds are simulated using the System of Atmospheric Modeling (SAM) [26], which is a non-hydrostatic, inelastic large eddy simulator (LES) [21, 39, 50]. It describes the turbulent atmosphere using equations of momentum, temperature, water mass balance and continuity. This model was coupled to a spectral (bin) microphysical model (HUJI SBM) [14, 25] of the droplets' size. It propagates the evolution of the droplet's size distribution by solving the equations for nucleation, diffusional growth, collision-coalescence and break-up. This is done on a logarithmic grid of 33 bins [ $2\mu\text{m}$ ,  $3.2\text{mm}$ ].

The simulation runs according to the BOMEX case [45] of trade wind cumulus clouds near Barbados. Humidity and potential temperature profiles are used as initial conditions, while the surface fluxes and large-scale forcing are constant. The mean horizontal background wind is zero. The horizontal boundary condition is cyclic. The domain is 5.12km long (cloud diameter is  $\approx 800\text{m}$ ) at 10m resolution. Vertically, the resolution is 10m from sea level to 3km, and then resolution coarsens to 50m. The cloud top reaches 2km. The simulation expresses an hour, of which 30 minutes includes the cloud's lifetime. The temporal resolution is 0.5sec.

We present results using two different time-varying clouds: *Cloud (i)* has size  $43 \times 30 \times 45$  voxels (See Fig. 4). *Cloud (ii)* has size  $60 \times 40 \times 45$  voxels (See Fig. 5). The voxel resolution is  $10m \times 10m \times 10m$ .

### 7.2. Rendered Measurements

Using the time-varying size distribution of the cloud droplets, Mie theory [6] provides the spatiotemporal extinction field  $\mathcal{B} = \{\beta_{t'}\}_{t' \in \mathcal{T}}$  and scattering phase function. The scene is irradiated by the sun, whose illumination angle changes in time, relative to the Earth's coordinates, while cameras overfly the evolving cloud. The solar trajectory in Earth coordinates corresponds to Feb/03/2013 at 13:54:30 - 14:01:00 local time, around 38N 123W. We tested several types of imaging setups:

*Setup A*: Three satellites orbit at 500km altitude, one after the other. Their velocity is 7.35km/sec. The orbital arc-length between nearest-neighboring satellites is 500km. At mid-time of the simulation,  $t = (t_1 + t_{N^{\text{state}}})/2$ , the setup is symmetric around the nadir direction. Then, the setup spans an angular range of  $114^\circ$ . Each satellite carries a perspective camera. The camera resolution is such that at nadir view, a pixel corresponds to 10m at sea level. Images are taken every 10sec, during 60sec, i.e.  $N^{\text{state}} = 7$ . This setup is illustrated in Fig. 6.

*Baseline*: The baseline uses all the accumulated 21 viewpoints of *Setup A*. However, all viewpoints here have perspective cameras that *simultaneously* acquire the cloud. In other words, this baseline is not prone to errors

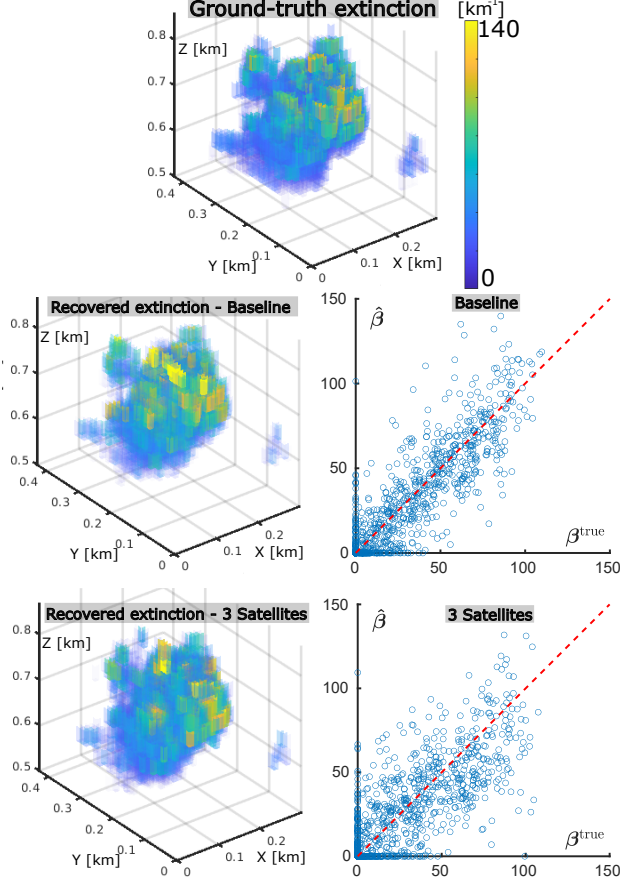


Figure 4: *Cloud (i)*. Results of recovery by the Baseline and Setup A are compared to the ground-truth by a 3D presentation and scatter plots that use 20% of the data points, randomly selected for display clarity.

that stem from temporal sampling. The baseline is used for recovery only at time  $t = (t_1 + t_{N^{\text{state}}})/2$ .

**Setup B:** This setup is similar to Setup A, but it uses only two satellites. Thus at mid-time of the simulation, the setup spans a  $57^\circ$  angular range.

**Setup C:** A single camera, similar to the Multi-angle Spectro-Polarimeter Imager (AirMSPI) [10], mounted on an aircraft flying  $154^\circ$  relative to North at 20km altitude. Imaging has a pushbroom scan geometry, having 10m spatial resolution at Nadir view and  $\lambda = 660\text{nm}$  wavelength band. AirMSPI scans view angles in a step-and-stare mode [10]. Based on AirMSPI PODEX campaign [9], we set 21 viewing angles along-track:  $\pm 65^\circ, \pm 62^\circ, \pm 58^\circ, \pm 54^\circ, \pm 50^\circ, \pm 44^\circ, \pm 38^\circ, \pm 30^\circ, \pm 21^\circ, \pm 11^\circ$  off-nadir and  $0^\circ$  (nadir). For example, three sample angles are illustrated in Fig. 7. It takes  $\approx 1\text{sec}$  to scan a cloud domain in any single view angle, during

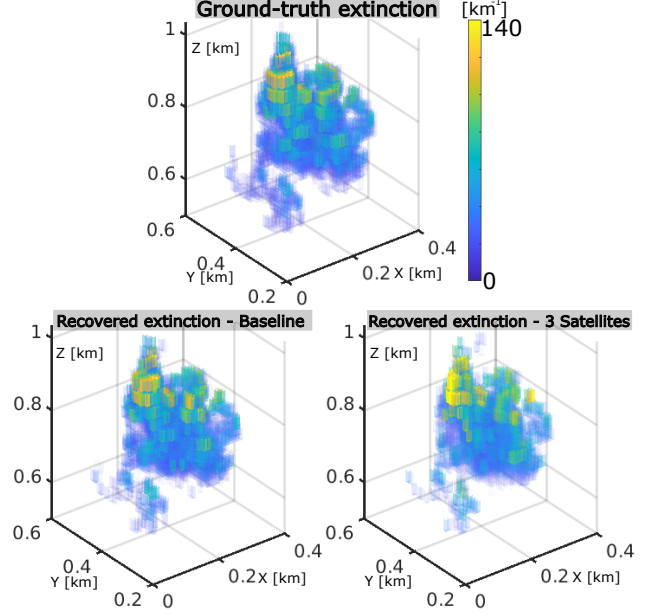


Figure 5: *Cloud (ii)* Results of recovery by the Baseline and Setup A are compared to the ground-truth.

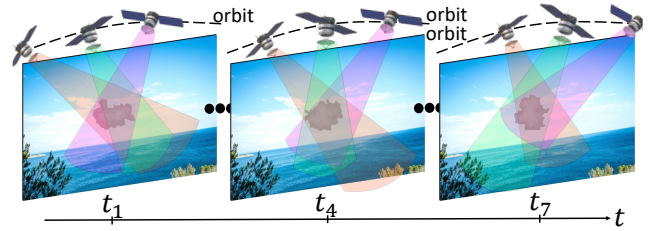


Figure 6: Illustration of Setup A.

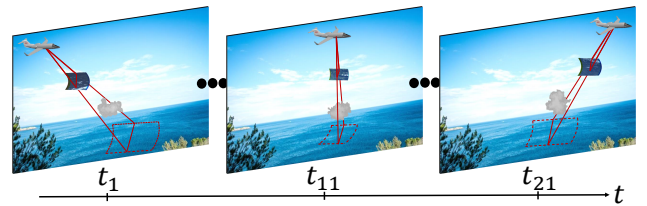


Figure 7: Illustration of Setup C. A domain is viewed at 21 pushbroom angles, sequentially.

which the cloud and solar directions are assumed constant. Dynamics are noticeable *between* view angles.

A spherical harmonic discrete ordinate method (SHDOM) code [13] provides the numerical forward model  $\mathcal{F}$ . Simulated measurements  $\{\mathbf{y}_t\}_{t \in \mathcal{T}}$  include noise. The noise model follows the AirMSPI sensors parameters [10, 46]. There, the sensor full-well depth is 200,000

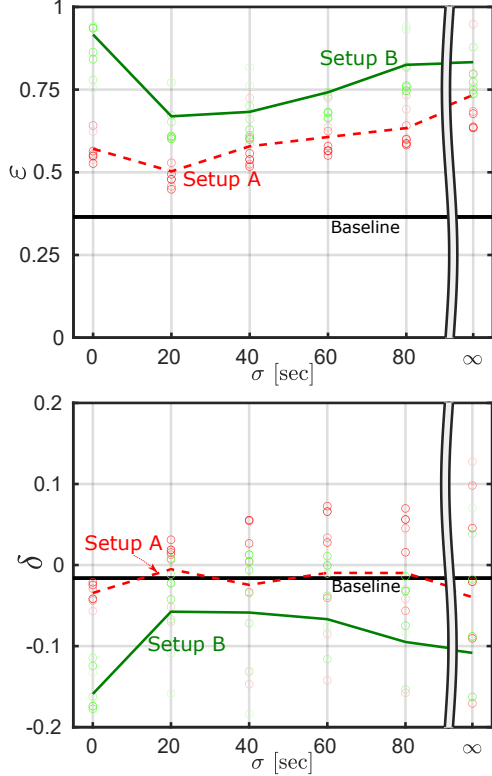


Figure 8: *Cloud (i)*. The criteria of Eq. (7) are marked by colored circles, whose saturation decays the farther the sampling time is from  $(t_1 + t_{N^{\text{state}}})/2$ . The criteria in Eq. (8) marked by solid or dashed lines, with corresponding colors. The setting  $\sigma = \infty$  refers to the solution by the state of the art, i.e. 3D static scattering tomography.

photo-electrons, readout noise has a standard deviation of 20 electrons, and the overall readout is quantized to 9 bits.

### 7.3. Tomography Results

The rendered and noisy images served as input to 4D tomographic reconstruction. The voxel size in the recovery was set to  $10\text{m} \times 10\text{m}$  horizontal,  $25\text{m}$  vertical and  $10\text{sec}$  resolution. For parallelization, optimization ran on a computer cluster, where each computer core was dedicated to rendering a modeled image from a distinct angle. The optimization was initialized by  $\{\beta_t\}_{t \in \mathcal{T}} = 1\text{km}^{-1}$ . Convergence was reached in several dozen iterations. Depending on the number of input images, it took between minutes to a couple of hours to complete, in total.

From Sec. 4, we assess that a value  $\sigma \sim 20\text{sec}$  is natural. Indeed, this is supported numerically in the plots of  $\varepsilon_t, \delta_t, \varepsilon, \delta$  for *Cloud (i)* (Fig 8). Analogous plots for *Cloud (ii)* are presented in the Appendix. The 3D tomographic results using Setup A are shown in Figs. 4 and 5, corresponding to *Cloud (i)* and *Cloud (ii)*. Both illustrate the state at  $t = (t_1 + t_{N^{\text{state}}})/2$ . Recovery used  $\sigma = 20\text{sec}$ .

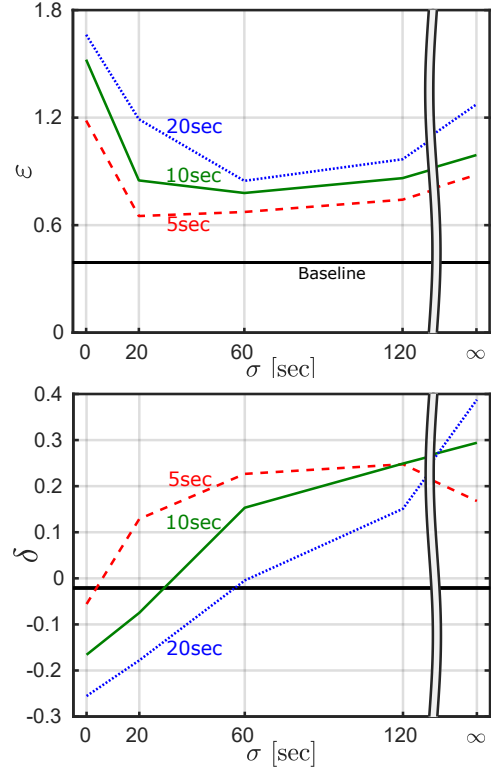


Figure 9: Setup C. Error measures (7) of *Cloud (i)* at time  $t = (t_1 + t_{N^{\text{state}}})/2$ , for different acquisition inter-angular temporal intervals. The setting  $\sigma = \infty$  refers to the solution by the state of the art, i.e. 3D static scattering tomography.

More results, particularly relating to Setup B are shown in the Appendix.

Setup C uses a single platform, which is challenging. Results depend significantly on how fast the aircraft flies, i.e. how long it takes to capture the cloud from a variety of angles (up to 21 angles). Fig. 9 compares the results for the recovery at  $t = (t_1 + t_{N^{\text{state}}})/2$  for inter-angle time interval of 5sec, 10sec and 20sec. As expected, quality ( $\varepsilon$ ) improves with velocity. Moreover, if the camera moves slowly (long time interval between angular samples), results improve by using a longer temporal support, observing the cloud from a wider angular range, despite its dynamics.

## 8. Experiment: Real World AirMSPI Data

We follow the experimental approach of [30], and use real-world data acquired by JPL's AirMSPI, which flies on board NASA's ER-2. The geometry is exactly as described in Setup C in Sec. 7.2, including location and time. We examine an atmospheric domain of size  $1.5\text{km} \times 2\text{km} \times 2\text{km}$  in the East-North-Up coordinates. We discretized the domain to  $80 \times 80 \times 80$  voxels. Because  $N^{\text{states}} = 21$ , the total number of unknowns is 10,752,000.

The inter-angle time interval in this experiment is around

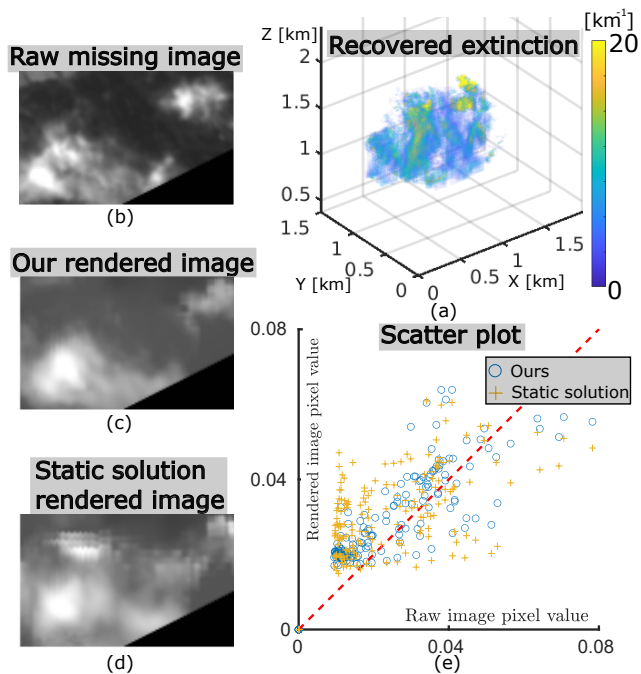


Figure 10: Recovered 3D extinction field using real data (a). A raw AirMSPI nadir image (b). Corresponding rendered views of a cloud, that was estimated using data that had excluded the nadir, either by our 4D CT approach (c) or current static 3D CT (d). Gamma correction was applied on (b,c,d) for display clarity. (e) A scatter plot of rendered vs. raw AirMSPI images at nadir.

20sec. Based on Fig. 9, we set  $\sigma = 60\text{sec}$  here. We want to focus on dynamic tomography of the evolving cloud, and not on global motion due to wind in the cloud field. Hence, we used the pre-processing approach of [30] to align the cloud images. Additionally, the ground albedo is estimated to be 0.04. The pre-processing and albedo estimation are described in the Appendix.

A recovered volumetric reconstruction for one time instant is displayed in Fig. 10. We have no ground-truth for the cloud content in this case. Hence we check for consistency using cross-validation. For this, we excluded the nadir image (Fig. 10b) from the recovery process. Thus tomography used 20 out of the 21 raw views. Afterward, we placed the recovered cloud in SHDOM physics-based rendering [13], to generate the missing nadir view. The result is then compared to the ground-truth missing view. Fig. 10 compares the result of this process for two solutions: our 4D tomographic solution, and the state-of-the-art, i.e., 3D static scattering tomography.

The same cross-validation process was repeated for the  $\pm 54^\circ$  view angles. Quantitatively, we measure the fitting error using Eq. (11). The results are summarized in Table (1).

	+54° view	nadir view	-54° view
Ours	0.96	0.38	0.24
Static solution	1.73	0.94	0.61

Table 1: Analysis of empirical data in different view angles. Quantitative fit (11) of our 4D result to the data, as compared to the error of state-of-the-art static 3D CT.

## 9. Discussion

We derive a framework for 4D CT of dynamic objects that scatter, using moving cameras. The natural temporal evolution of an object indicates the temporal and angular sampling needed for a good reconstruction. Given these conditions, 4D CT recovery can be done, even with a small number of cameras. We believe that our approach can be relevant in additional tomographic setups [19] that rely on radiative transfer. Some elements of this work are generic, beyond scattering CT. Thus, it is worth applying the approach to other tomographic modalities. Our findings can significantly improve various research fields, including biomedical CT, flow imaging and atmospheric sciences.

## Acknowledgment

We are grateful to Aviad Levis and Jesse Loveridge for the pySHDOM code and for being responsive to questions about it. We are grateful to Vadim Holodovsky and Omer Shubi for helping in setting elements of the code. We thank the following people: Ilan Koren, Orit Altaratz and Yael Sde-Chen for useful discussions and good advice; Danny Rosenfeld for pointing out Ref. [15] to us, Johanan Erez, Ina Talmon and Daniel Yagodin for technical support. Yoav Schechner is the Mark and Diane Seiden Chair in Science at the Technion. He is a Landau Fellow - supported by the Taub Foundation. His work was conducted in the Orlendorff Minerva Center. Minvera is funded through the BMBF. This project has received funding from the European Union’s Horizon 2020 research and innovation programme under grant agreement No 810370-ERC-CloudCT.

## Appendices

We now present several appendices. Appendix A elaborates on pre-processing which is applied to real world measurements that are presented in Sec. 8. This data was collected by the AirMSPI instrument. Appendix B provides an additional example of the bandwidth of the power spectrum of a cloud and more simulation results. Appendix C analyzes the computational complexity of the method.



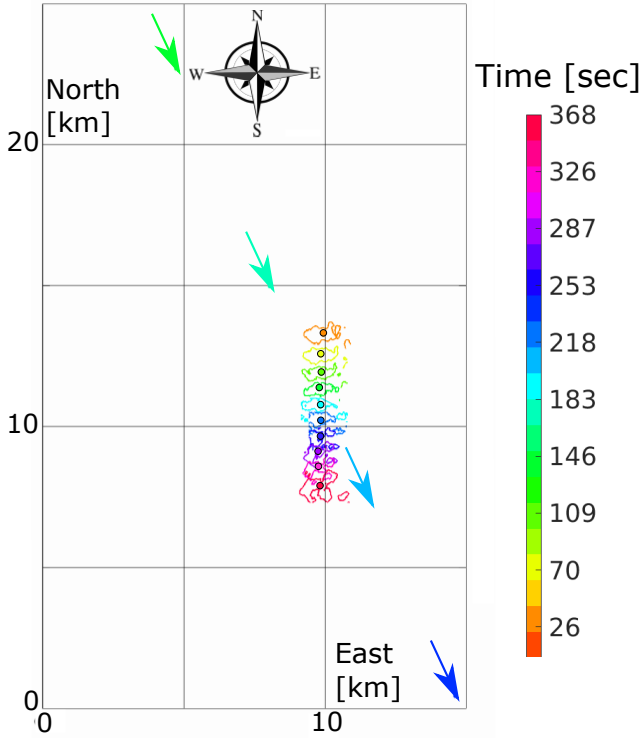


Figure 11: Geometry of the AirMSPI real world setup which led to the data presented in Sec. 8. The color represents the locations of the cloud and the AirMSPI instrument in the different time states. The cloud’s outer contour and its corresponding center of mass, marked in a circle, are presented per state. The AirMSPI location and velocity are marked by arrows. The arrows point to the AirMSPI flight direction azimuth of  $154^\circ$  relative to the North. Due to the domain size, not all AirMSPI locations are illustrated here. Due to wind, the cloud moves at 57km/h in azimuth  $182^\circ$  relative to the North.

## A. Pre-processing Real World Data

Sec. 8 presents results using real world measurements. The data were acquired by the AirMSPI instrument. As explained in Sec. 8, while AirMSPI flies, clouds move due to wide-scale wind at their altitude. The geometry of AirMSPI’s path and the cloud drift during the experiment is presented in Fig. 11. In order to eliminate the influence of wide-scale wind, a registration process of the cloud images is done. Moreover, for tomographic recovery, we need to have an assessment of the Earth surface albedo, under the clouds. This section describes how pre-processing estimates the wind and albedo.

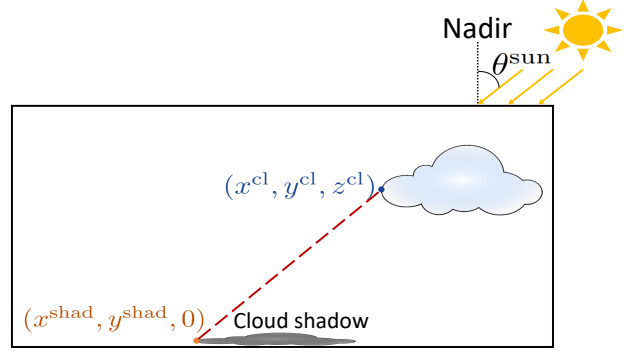


Figure 12: Illustration of estimation of cloud altitude using its shadow.

### A.1. Wind Estimation

Clouds are segmented from the surface automatically [47]. Cloudy pixels are then used to estimate the cloud center of mass in each image [30]. A registration of these centers of mass can be done by triangulation. However, triangulation of images of a moving object using a translating camera has an inherent ambiguity. This ambiguity can be solved if the cloud height is known. In this work, we assess this altitude of a cloud by its shadow [1, 20, 32]. Let  $(x^{cl}, y^{cl}, z^{cl})$  and  $(x^{shad}, y^{shad}, 0)$  be a point in a cloud and its corresponding shadow point on the earth surface, respectively (see Fig. 12). Let  $r^{shad} = \sqrt{(x^{cl} - x^{shad})^2 + (y^{cl} - y^{shad})^2}$ . We obtain  $x^{cl}, y^{cl}, x^{shad}$  and  $y^{shad}$  from the AirMSPI images. Given the solar zenith angle relative to the nadir  $\theta^{sun}$ , the altitude  $z^{cl}$  satisfies

$$z^{cl} = \frac{r^{shad}}{\tan(\theta^{sun})}. \quad (18)$$

For the example shown in Sec. 8, we estimated the cloud base height as  $\approx 500\text{m}$  and its top at  $\approx 1100\text{m}$ . Indeed taking MODIS/AQUA [3] retrievals of cloud top heights, indicates that the clouds’ top in the region<sup>1</sup> does not exceed 1000m, which makes our approximation reasonable.

We approximate the cloud horizontal velocity by projecting the images from the locations of the camera to the altitude of  $z^{cl}$ . From the center of mass of these images, we assess the velocity. We register the camera locations so the projections of the center of mass of all images intersect at the same point at altitude of  $z^{cl}$ . The images and the registered camera locations are the input for 4D recovery.

### A.2. Surface Albedo Estimation

3D radiative transfer calculations require the surface albedo. We use non-cloudy pixels to estimate the albedo.

<sup>1</sup>This data applies over the coast of California, 38N 122W, on Feb/03/2013 at 13:30 local time.

Let  $\mathcal{Y}$  be a set of non-cloudy pixels. We estimate the surface albedo  $a$  as,

$$\hat{a} = \operatorname{argmin}_a \sum_{y \in \mathcal{Y}} \|y - \mathcal{F}(\beta^{\text{air}}; a)\|_2^2. \quad (19)$$

Here  $\mathcal{F}(\beta^{\text{air}}; a)$  is a rendering (forward) model where the surface albedo is set to be  $a$  and the atmospheric medium contains no clouds. That is, sunlight interacts only with the air and the surface. Scattering by air is assumed to be known [17, 48]. The optimization problem is solved by the Brent minimization method [8], implemented by the SciPy package [44]. For the example shown in Sec. 8, the surface albedo is estimated to be 0.04.

## B. Additional Simulations

### B.1. Cloud Temporal Spectrum

Sec. 4 indicates that the temporal power spectrum of a convective cloud at 10m resolution is effectively limited. Thus, a temporal sampling period of 25[sec] or shorter is required. We assess this in an additional cloud simulation. We conducted a single cloud simulation in high resolution, using small changes, relative to the simulation described in Sec. 7.1. The simulation parameters and setting are similar. However, the perturbation that initiates the convection and turbulent flow has a smaller horizontal size. This creates a smaller cloud with a horizontal width of  $\approx 400\text{m}$ . This cloud is more sensitive to mixing and evaporation than the cloud in Sec. 7.1 whose width is  $\approx 800\text{m}$ . Because mixing with the environment is more intense here, the clouds' growth is inhibited. It can not exceed a height of 1400m, compared to a 2000m ceiling of the cloud in Sec. 7.1.

Using the same process described in Sec. 4, the temporal power spectrum of the cloud is presented in Fig. 13. The cutoff frequency is  $\approx 1/70[\text{Hz}]$ , and it is not sensitive to the evolving stages of the cloud. Here the required temporal sampling period is 35[sec] or shorter. This is more tolerable compared to the temporal sampling period in Sec. 4.

### B.2. Additional Tomography Results

Recall that our method is demonstrated on two simulated clouds, *Cloud (i)* and *Cloud (ii)*, using several types of imaging setups: Setup A, Setup B and Baseline. Moreover, recall the error criteria as Eqs. (7,8). Fig. 14 shows  $\varepsilon_t, \delta_t, \varepsilon, \delta$  for *Cloud (ii)*. It reinforces the assessment that a value  $\sigma \sim 20\text{sec}$  is natural, as explained in Sec. 4. Figs. 15 and 16 respectively visualize the results of *Cloud (i)* and *Cloud (ii)*. The 3D cut-sections of the error  $|\beta_t^{\text{true}}(\mathbf{x}) - \hat{\beta}_t(\mathbf{x})|$  at  $t = (t_1 + t_{N^{\text{state}}})/2$  is presented for Setup A, Setup B and Baseline in Figs. 15 and 16[Top]. Fig. 16[Bottom] uses scatter plots to compare the ground-truth to the results obtained by either the Baseline, Setup A or Setup B.

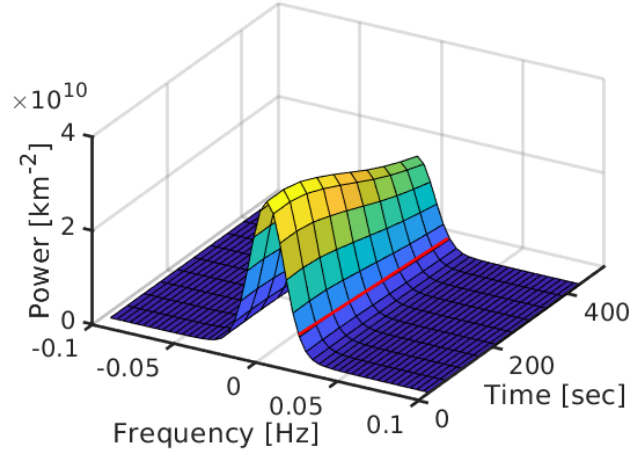


Figure 13: A cutoff frequency  $\approx 1/70[\text{Hz}]$ , within which 95% of the signal power is contained, is marked in red.

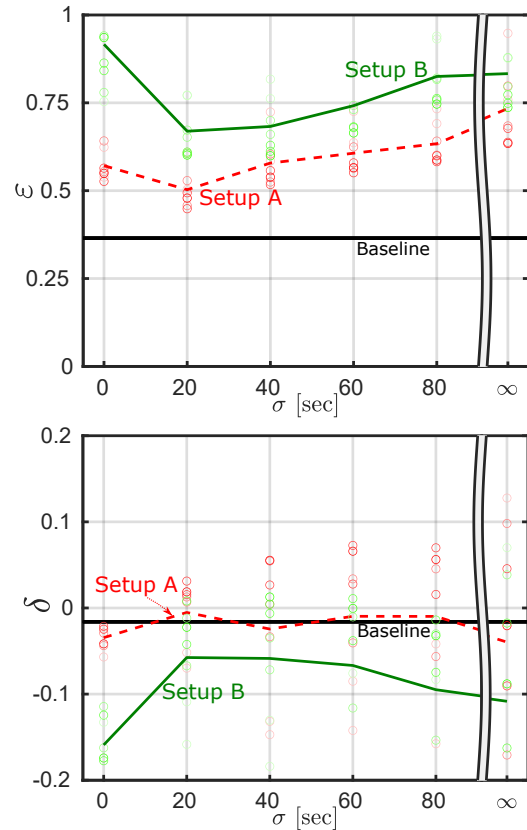


Figure 14: *Cloud (ii)*. The criteria of Eq. (7) are marked by colored circles, whose saturation decays the farther the sampling time is from  $(t_1 + t_{N^{\text{state}}})/2$ . The criteria in Eq. (8) are marked by solid or dashed lines, with corresponding colors. The setting  $\sigma = \infty$  refers to the solution by the state of the art, i.e. 3D static scattering tomography.

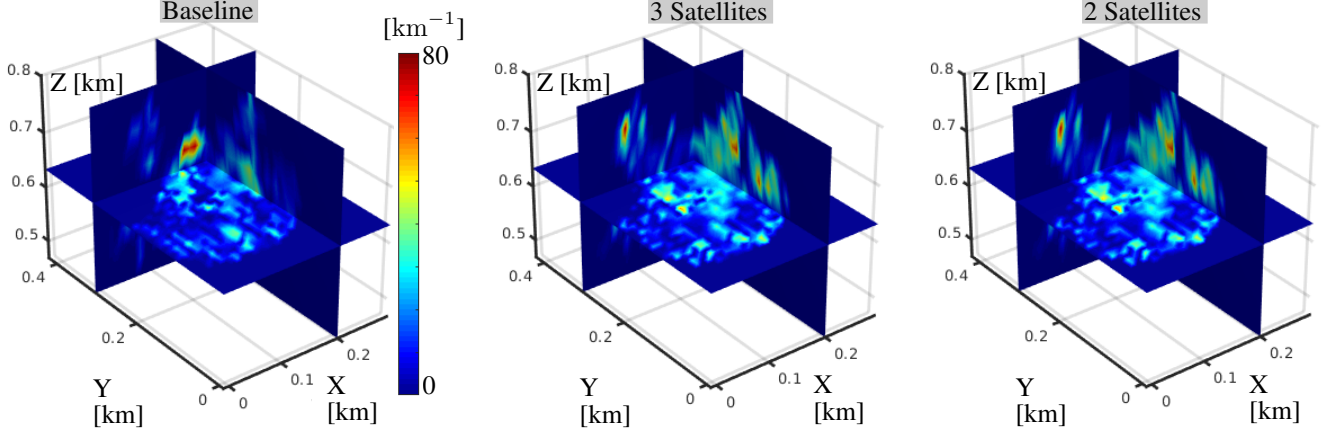


Figure 15: *Cloud (i)*. 3D cut-sections of the error  $|\beta_t^{\text{true}}(\mathbf{x}) - \hat{\beta}_t(\mathbf{x})|$  at  $t = (t_1 + t_{N^{\text{state}}})/2$  for Baseline, Setup A and Setup B.

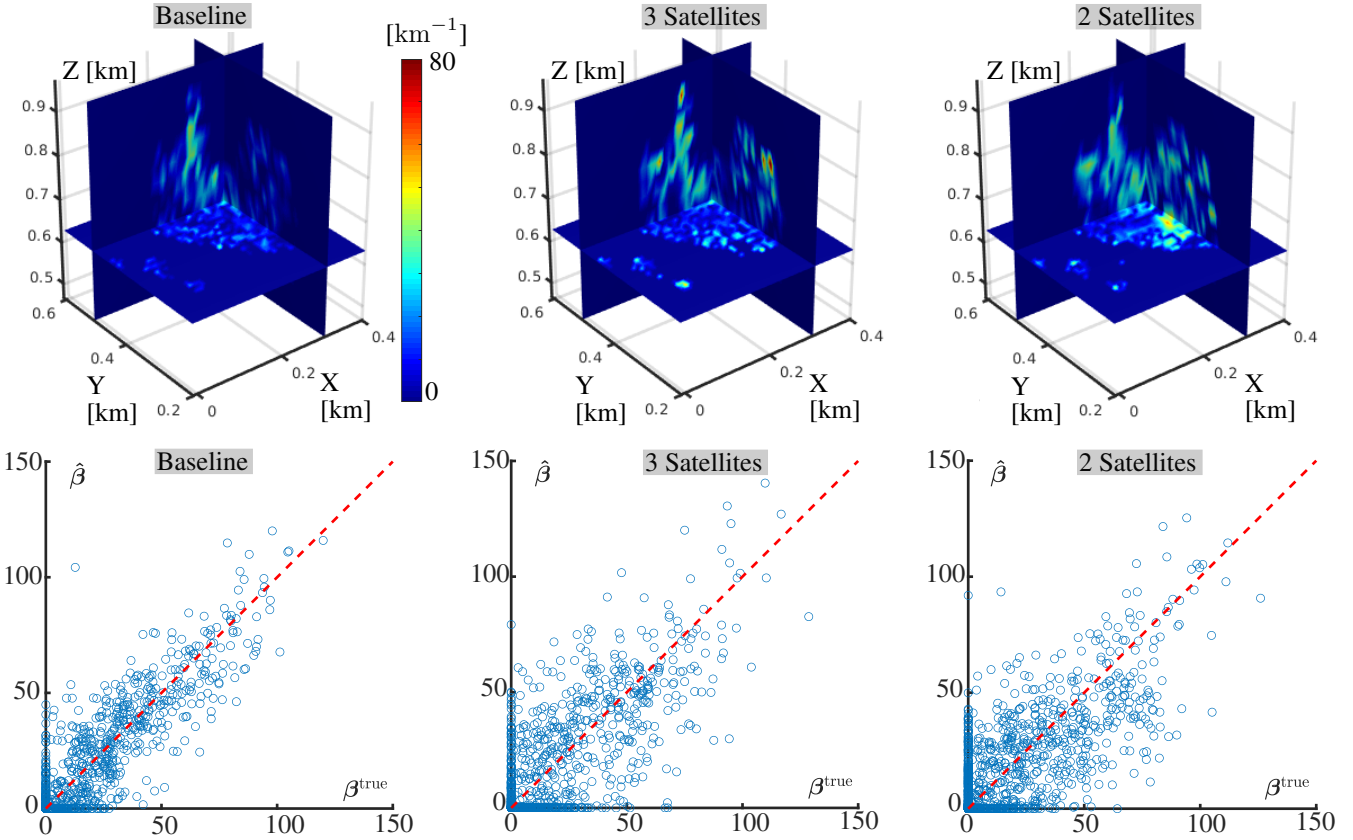


Figure 16: *Cloud (ii)* comparison for Baseline, Setup A and Setup B. [Top] 3D cut-sections of the error  $|\beta_t^{\text{true}}(\mathbf{x}) - \hat{\beta}_t(\mathbf{x})|$  at  $t = (t_1 + t_{N^{\text{state}}})/2$ . [Bottom] Scatter plots that use randomly selected 20% of the data points, for display clarity.

### C. Computational Complexity

The time complexity for solving the 4D CT inverse problem, (Eq. 10) is governed by the gradient calculation. Recall

the formulation of the approximate gradient,

$$\mathbf{g}_t(\boldsymbol{\beta}) = \sum_{t' \in \mathcal{T}} w_{t'}(t) [\mathcal{F}(\boldsymbol{\beta}_{t'}) - \mathbf{y}_{t'}] \frac{\partial \mathcal{F}(\boldsymbol{\beta}_{t'})}{\partial \boldsymbol{\beta}_{t'}}. \quad (20)$$

Computing the Jacobian  $\partial\mathcal{F}(\beta_{t'})/\partial\beta_{t'}$  is complex, thus it is established numerically by a surrogate function that evolves through iterations [30, 33]. Calculating the gradient includes two dominant time-consuming processes that are executed in alternation. The first process calculates the forward model for the  $N^{\text{state}}$  cloud states  $\{\mathcal{F}(\beta_{t'})\}_{t' \in \mathcal{T}}$ . The second process sums over the entire set of measurements, which does not depend on the number of cloud states that we seek to recover.

A spherical harmonic discrete ordinate method (SHDOM) code is used for computing the numerical forward model  $\mathcal{F}(\cdot)$  and the Jacobian. SHDOM iteratively updates the estimation of 3D radiation fields until convergence. Calculating the forward model for the  $N^{\text{state}}$  cloud states can be done in parallel. Thus, the time complexity is governed by the temporal state for which the SHDOM code takes the longest time to compute the forward model. By calculating the forward model for all cloud states in parallel, the time complexity of gradient calculation is insensitive to the number of cloud states  $N^{\text{state}}$ .

As a numerical example, we used 20 iterations of the L-BFGS-B optimization. Using measurements of *Cloud (i)* acquired by Setup A, the run-time of the solution by our method was 501[sec]. The static solution took 301[sec]. In both, the computer was Intel® Xeon® Gold 6240 CPU @ 2.60GHz with 72 cores. Although our method recovers  $N^{\text{state}} = 7$  times more voxels, the run-time is less than twice that of the static solution. The time difference is caused by overheads of saving and loading larger data with our method, and nonoptimal task division for the cores.

## References

[1] Austin Abrams, Kyla Miskell, and Robert Pless. The episolar constraint: Monocular shape from shadow correspondence. In *Proc. IEEE CVPR*, pages 1407–1414, 2013. 9

[2] David A Agard, Yasushi Hiraoka, Peter Shaw, and John W Sedat. Fluorescence microscopy in three dimensions. *Methods in cell biology*, 30:353–377, 1989. 4

[3] NASA Federal agency. *NASA Earth Data Site*. <https://worldview.earthdata.nasa.gov/>. 9

[4] Amit Aides, Aviad Levis, Vadim Holodovsky, Yoav Y Schechner, Dietrich Althausen, and Adi Vainiger. Distributed sky imaging radiometry and tomography. In *Proc. IEEE ICCP*, pages 1–12, 2020. 1, 2

[5] Rushil Anirudh, Hyojin Kim, Jayaraman J Thiagarajan, K Aditya Mohan, Kyle Champley, and Timo Bremer. Lose the views: Limited angle ct reconstruction via implicit sinogram completion. In *Proc. IEEE CVPR*, pages 6343–6352, 2018. 1

[6] Craig F Bohren and Donald R Huffman. *Absorption and scattering of light by small particles*. John Wiley & Sons, 2008. 5

[7] Stacey W Boland, David J Diner, John C Pearson, and Kevin A Burke. NASA’s Multi-Angle Imager for Aerosols

(MAIA) earth venture instrument investigation. *AGUFM*, 2018:GH41C–1443, 2018. 2

[8] Richard P Brent. *Algorithms for minimization without derivatives*. Courier, 2013. 10

[9] David J Diner, Michael J Garay, Olga V Kalashnikova, Brian E Rheingans, Sven Geier, Michael A Bull, Veljko M Jovanovic, Feng Xu, Carol J Bruegge, Anthony B Davis, et al. Airborne multiangle spectropolarimetric imager (AirMSPI) observations over California during NASA’s polarimeter definition experiment (PODEX). In *Polarization Science and Remote Sensing VI*, volume 8873, page 88730B. SPIE, 2013. 6

[10] David J Diner, Feng Xu, Michael J Garay, John V Martonchik, Brian E Rheingans, Sven Geier, Anthony B Davis, BR Hancock, Michael A Jovanovic, Veljko M and Bull, et al. The Airborne Multiangle Spectropolarimetric Imager (AirMSPI): a new tool for aerosol and cloud remote sensing. *Atmos. Meas. Tech.*, 6(8):2007, 2013. 2, 6

[11] Marie L Eckert, Wolfgang Heidrich, and Nils Thuerey. Coupled fluid density and motion from single views. In *Computer Graphics Forum*, volume 37, pages 47–58. Wiley Online Library, 2018. 1

[12] K Franklin Evans. The spherical harmonics discrete ordinate method for three-dimensional atmospheric radiative transfer. *Journal of the Atmospheric Sciences*, 55(3):429–446, 1998. 2

[13] K Franklin Evans and WJ Wiscombe. Improvements to the SHDOM radiative transfer modeling package. In *Proc. 13th ARM Sci. Team Meeting*, 2003. 6, 8

[14] Jiwen Fan, Mikhail Ovtchinnikov, Jennifer M Comstock, Sally A McFarlane, and Alexander Khain. Ice formation in Arctic mixed-phase clouds: Insights from a 3-D cloud-resolving model with size-resolved aerosol and cloud microphysics. *JGR: Atmospheres*, 114(D4), 2009. 5

[15] TT Fujita. Mesoscale classifications: their history and their application to forecasting. In *Mesoscale meteorology and forecasting*, pages 18–35. Springer, 1986. 2, 3, 8

[16] Ioannis Gkioulekas, Anat Levin, and Todd Zickler. An evaluation of computational imaging techniques for heterogeneous inverse scattering. In *ECCV*, pages 685–701. Springer, 2016. 1

[17] Howard R Gordon, James W Brown, and Robert H Evans. Exact Rayleigh scattering calculations for use with the Nimbus-7 coastal zone color scanner. *Applied Optics*, 27(5):862–871, 1988. 10

[18] James Gregson, Michael Krimmerman, Matthias B Hullin, and Wolfgang Heidrich. Stochastic tomography and its applications in 3D imaging of mixing fluids. *ACM TOG*, 31(4):1–10, 2012. 1

[19] Jörg Gumbel, Linda Megner, Ole Martin Christensen, Nickolay Ivchenko, Donal P Murtagh, Seunghyuk Chang, Joachim Dillner, Terese Ekebrand, Gabriel Giono, Arvid Hammar, et al. The MATS satellite mission—gravity wave studies by mesospheric airglow/aerosol tomography and spectroscopy. *Atmospheric Chemistry and Physics*, 20(1):431–455, 2020. 8

- [20] Michael Hatzitheodorou and John R Kender. An optimal algorithm for the derivation of shape from shadows. In *Proc. IEEE CVPR*, pages 486–487, 1988. 9
- [21] Thijs Heus, Harm JJ Jonker, Harry EA Van den Akker, Eric J Griffith, Michal Koutek, and Frits H Post. A statistical approach to the life cycle analysis of cumulus clouds selected in a virtual reality environment. *JGR: Atmospheres*, 114(D6), 2009. 5
- [22] Harish P Hiriyannaiah. X-ray computed tomography for medical imaging. *IEEE signal Processing magazine*, 14(2):42–59, 1997. 1
- [23] Vadim Holodovsky, Yoav Y Schechner, Anat Levin, Aviad Levis, and Amit Aides. In-situ multi-view multi-scattering stochastic tomography. In *Proc. IEEE ICCP*, pages 1–12, 2016. 4
- [24] Anders P Kaestner, Beat Munch, and Pavel Trtik. Spatiotemporal computed tomography of dynamic processes. *Optical Engineering*, 50(12):123201, 2011. 1
- [25] A Khain, A Pokrovsky, M Pinsky, A Seifert, and Vaughan Phillips. Simulation of effects of atmospheric aerosols on deep turbulent convective clouds using a spectral microphysics mixed-phase cumulus cloud model. Part I: Model description and possible applications. *JAS*, 61(24):2963–2982, 2004. 5
- [26] Marat F Khairoutdinov and David A Randall. Cloud resolving modeling of the ARM summer 1997 IOP: Model formulation, results, uncertainties, and sensitivities. *JAS*, 60(4):607–625, 2003. 5
- [27] Kiriakos N Kutulakos and Steven M Seitz. A theory of shape by space carving. *IJCV*, 38(3):199–218, 2000. 5
- [28] Vincent Leroy, Jean-Sébastien Franco, and Edmond Boyer. Multi-view dynamic shape refinement using local temporal integration. In *Proc. IEEE ICCV*, pages 3094–3103, 2017. 2
- [29] Aviad Levis, Jesse Loveridge, and Amit Aides. *Pyshdom*. 2020. Available online. <https://github.com/aviadlevis/pyshdom>. 2
- [30] Aviad Levis, Yoav Y Schechner, Amit Aides, and Anthony B Davis. Airborne three-dimensional cloud tomography. In *Proc. IEEE ICCV*, pages 3379–3387, 2015. 2, 4, 5, 7, 8, 9, 12
- [31] Aviad Levis, Yoav Y Schechner, and Anthony B Davis. Multiple-scattering microphysics tomography. In *Proc. IEEE CVPR*, pages 6740–6749, 2017. 2, 5
- [32] Gregoris Liasis and Stavros Stavrou. Satellite images analysis for shadow detection and building height estimation. *ISPRS Journal of Photogrammetry and Remote Sensing*, 119:437–450, 2016. 9
- [33] Tamar Loeub, Aviad Levis, Vadim Holodovsky, and Yoav Y Schechner. Monotonicity prior for cloud tomography. In *Proc. ECCV*, pages 24–29, 2020. 2, 4, 5, 12
- [34] Fernando Macias-Garza, Kenneth R Diller, and Alan C Bovik. Missing cone of frequencies and low-pass distortion in three-dimensional microscopic images. *Optical Engineering*, 27(6):276461, 1988. 4
- [35] Bernhard Mayer. Radiative transfer in the cloudy atmosphere. In *EPJ Web of Conferences*, volume 1, pages 75–99. EDP Sciences, 2009. 2
- [36] Brent A McBride, J Vanderlei Martins, Henrique MJ Barbosa, William Birmingham, and Lorraine A Remer. Spatial distribution of cloud droplet size properties from Airborne Hyper-Angular Rainbow Polarimeter (AirHARP) measurements. *AMT*, 13(4):1777–1796, 2020. 2
- [37] Armin Mustafa, Hansung Kim, Jean-Yves Guillemaut, and Adrian Hilton. Temporally coherent 4D reconstruction of complex dynamic scenes. In *Proc. IEEE CVPR*, pages 4660–4669, 2016. 2
- [38] Srinivasa G Narasimhan, Shree K Nayar, Bo Sun, and Sanjeev J Koppal. Structured light in scattering media. In *Proc. IEEE ICCV*, volume 1, pages 420–427, 2005. 1
- [39] RAJ Negggers, HJJ Jonker, and AP Siebesma. Size statistics of cumulus cloud populations in large-eddy simulations. *JAS*, 60(8):1060–1074, 2003. 5
- [40] Tim L Neilsen, Jose-Vanderlei Martins, RA Fernandez Borda, Cameron Weston, Crystal Frazier, Dominik Cieslak, and Kevin Townsend. The Hyper-Angular Rainbow Polarimeter (HARP) CubeSat Observatory and the Characterization of Cloud Properties. In *AGU Fall Meeting Abstracts*, volume 2015, pages A43A–0237, 2015. 2
- [41] Tinsu Pan, Ting-Yim Lee, Eike Rietzel, and George TY Chen. 4D-CT imaging of a volume influenced by respiratory motion on multi-slice CT. *Medical physics*, 31(2):333–340, 2004. 1, 2
- [42] Yiming Qian, Minglun Gong, and Yee-Hong Yang. Stereo-based 3D reconstruction of dynamic fluid surfaces by global optimization. In *Proc. IEEE CVPR*, pages 1269–1278, 2017. 1, 2
- [43] Klaus Schilling, Yoav Y Schechner, and Ilan Koren. CloudCT - computed tomography of clouds by a small satellite formation. In *Proc. IAA symposium on Small Satellites for Earth Observation*, 2019. 2
- [44] The SciPy community. *SciPy*. 2020. Available online. [https://docs.scipy.org/doc/scipy/reference/generated/scipy.optimize.minimize\\_scalar.html](https://docs.scipy.org/doc/scipy/reference/generated/scipy.optimize.minimize_scalar.html). 10
- [45] A Pier Siebesma, Christopher S Bretherton, Andrew Brown, Andreas Chlond, Joan Cuxart, Peter G Duynkerke, Hongli Jiang, Marat Khairoutdinov, David Lewellen, Chin-Hoh Moeng, et al. A large eddy simulation intercomparison study of shallow cumulus convection. *JAS*, 60(10):1201–1219, 2003. 5
- [46] Gerard Van Harten, David J Diner, Brian JS Daugherty, Brian E Rheingans, Michael A Bull, Felix C Seidel, Russell A Chipman, Brian Cairns, Andrzej P Wasilewski, and Kirk D Knobelspiesse. Calibration and validation of airborne multiangle spectropolarimetric imager (AirMSPI) polarization measurements. *Applied Optics*, 57(16):4499–4513, 2018. 6
- [47] Flavio R Velasco. Thresholding using the ISODATA clustering algorithm. Technical report, Univ. of Maryland College Park, Computer Science Center, 1979. 9
- [48] Menghua Wang. A refinement for the Rayleigh radiance computation with variation of the atmospheric pressure. *International Journal of Remote Sensing*, 26(24):5651–5663, 2005. 10

- [49] TE Wright, M Burton, DM Pyle, and T Caltabiano. Scanning tomography of SO<sub>2</sub> distribution in a volcanic gas plume. *Geophysical research letters*, 35(17), 2008. [1](#)
- [50] Huiwen Xue and Graham Feingold. Large-eddy simulations of trade wind cumuli: Investigation of aerosol indirect effects. *JAS*, 63(6):1605–1622, 2006. [5](#)
- [51] Guangming Zang, Ramzi Idoughi, Ran Tao, Gilles Lubineau, Peter Wonka, and Wolfgang Heidrich. Space-time tomography for continuously deforming objects. *ACM Trans. Graph.*, 37, 2018. [1](#)
- [52] Guangming Zang, Ramzi Idoughi, Ran Tao, Gilles Lubineau, Peter Wonka, and Wolfgang Heidrich. Warp-and-project tomography for rapidly deforming objects. *ACM TOG*, 38(4):1–13, 2019. [1](#)
- [53] Guangming Zang, Ramzi Idoughi, Congli Wang, Anthony Bennett, Jianguo Du, Scott Skeen, William L Roberts, Peter Wonka, and Wolfgang Heidrich. Tomofluid: Reconstructing Dynamic Fluid from Sparse view videos. In *Proc. IEEE CVPR*, pages 1870–1879, 2020. [1](#)
- [54] Ciyou Zhu, Richard H Byrd, Peihuang Lu, and Jorge Nocedal. Algorithm 778: L-BFGS-B: Fortran subroutines for large-scale bound-constrained optimization. *ACM TOMS*, 23(4):550–560, 1997. [5](#)